Article

Mitigating Anisotropic Changes in Classical Layered Oxide Materials by Controlled Twin Boundary Defects for Long Cycle Life Li-Ion Batteries

Published as part of the Virtual Special Issue "John Goodenough at 100".

Hyeseung Chung, Yixuan Li, Minghao Zhang,* Antonin Grenier, Carlos Mejia, Diyi Cheng, Baharak Sayahpour, Chengyu Song, Meghan Hannah Shen, Ricky Huang, Erik A. Wu, Karena W. Chapman, Suk Jun Kim,* and Y. Shirley Meng*

Read Online

ACCESS | Metrics & More | Article Recommendations | Supporting Information

ABSTRACT: The classical layered NMC oxides Li-$Ni_xMn_yCo_{1-x-y}O_2$ ($0 < (x,y) < 1$) are promising high energy density cathodes for Li-ion batteries. However, their inherent structure instability at the highly delithiated state causes capacity degradation as cycling proceeds. Here, we report a mitigating strategy for addressing the capacity decay problem in multiple classical NMC materials through the design of controlled twin boundary defects. The radially aligned twin boundary defects are engineered in nanosized NMC cathodes through polyol synthesis. The crystallographic orientation of each subgrain rotates across the twin boundaries, and the particles have maximum exposure to the electrolyte with the (003) planes (which are more stable than other planes). Increased cation disorder and the formation of

rocksalt-like phase are consistently observed along the twin boundaries through scanning transmission electron microscopy (STEM), acting as a rigid framework that mitigates anisotropic changes in NMC during cycling. *Operando* X-ray diffraction confirms this hypothesis as the degree of anisotropic changes is minimized in NMC with twin boundaries. The synthesized NMC materials with twin boundary defects exhibits enhanced electrochemical performance compared to the corresponding microsized materials with identical composition. The twin boundary defects engineering in NMC structure can effectively suppress the phase transformation and material degradation, serving as a novel and universal approach in designing stable intercalation compounds for high voltage long-cycle life Li-ion batteries.
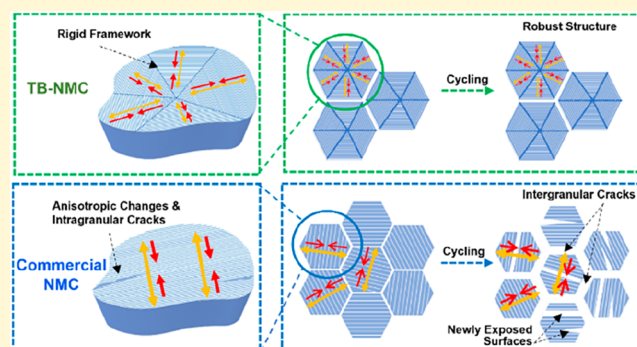
INTRODUCTION

Li-ion battery (LIB) technology holds the key to the future of electric vehicles (EVs) as cost, safety, driving range, and battery lifetime are determining factors of a user's experiences with EVs.[1] Among the existing cathodes in LIBs, $LiNi_xMn_yCo_{1-x-y}O_2$ (NMC) is one of the most popular choices in the EV market due to their high reversible capacity, good rate capability, and relatively low cost. Dahn's group showed that an NMC/graphite cell has the ability to power an EV for over 1 million miles, suggesting that driverless robotaxis, long haul trucks, and city buses can be potentially powered by batteries.[2] The energy density in NMC can be further improved by delithiating the cathode using a higher voltage cutoff (>4.5 V), but the inherent structural instability of NMC in such a highly delithiated state will accelerate material degradation and compromise the cycle life.[3,4] For instance, highly delithiated NMC yields large amounts of Ni^{4+} with high reactivity, which easily reduces to the more stable

rocksalt-like NiO structure (especially on the surface of the particles), hindering Li diffusion pathways as cycling proceeds.[5,6] Parasitic side reactions between the electrode and electrolyte are also accelerated in high voltage such as HF corrosion on electrode−electrolyte interphases and transition metal (TM) dissolution from NMC and redeposition on the graphite.[7,8] Furthermore, anisotropic volume expansion (contraction) in NMC during Li intercalation (deintercalation) leads to disintegration and contact loss between the cathode active material, conductive carbon black, and the current
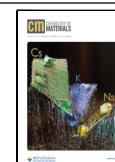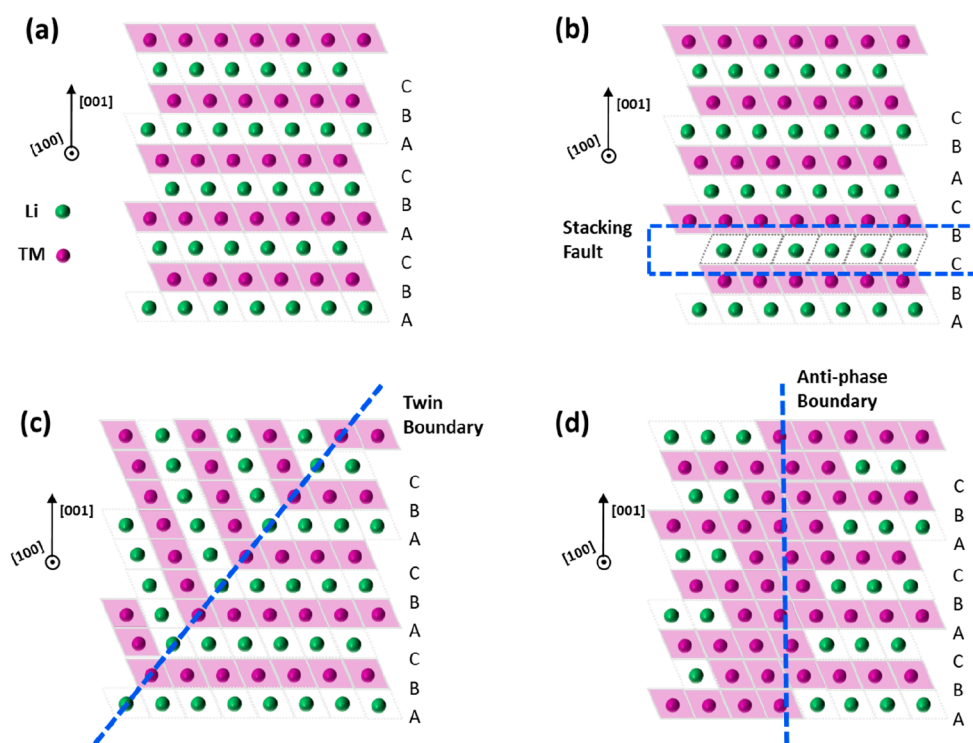
Figure 1. Side-view schematics of layered oxide crystals without defects and with different types of defects. (a) No defects; (b) stacking fault defect; (c) twin boundary defect; (d) antiphase boundary defect. Li ions are green circles, and TM ions are purple circles. LiO$_6$ and TMO$_6$ octahedra are depicted as parallelograms with Li or TM in the center.

collector at high voltage.[9] Additionally, cracks can form within the NMC secondary particles and propagate through the primary particle boundaries.[10] Such progressive intergranular separation results in the eventual loss of electrical contact, which promotes infiltration of electrolyte along the grain boundaries into the particle interior and accelerates surface degradation as well as Li inventory loss, eventually leading to the capacity fade.

Over the past few decades, diverse strategies have been adopted to overcome some of these disadvantages in NMC, including lattice doping, surface modification, tuning the material composition, synthesizing in single crystals forms, and building concentration gradient architectures.[2,5,11,12] However, designing structure defects in NMC such as controlled twin boundaries (TB) were often time neglected as a mitigating strategy to achieve better cycling performance. In this work, the unique properties of controlled TB defects in the as-synthesized NMC layered materials will be studied in the following sections, especially the enhanced surface stability and structure robustness in NMC at high voltage cycling. Previous literature mainly focused on the negative effects of many different types of defects generated during electrochemical cycling. For example, Li/Ni mixing (or named as Li/Ni antisite defect) is a common defect in layered materials which hinders Li transport during cycling and causes capacity decay.[13] At high voltage cycling, the formation of dislocation network was also reported in Li-rich NMC layered oxides and recognized as one of the origins for voltage fade.[14] Stacking faults (SF, lateral displacements of the layers) were also reported to cause sluggish Li diffusion in layered oxides and lead to electrochemical irreversibility over cycling.[15] In addition, antiphase boundaries (APB) and TB were reported to propagate after cycling, resulting in the increase of cation disordering and increased resistance for Li ion extraction and intercalation.[16]

Although SF, APB, and TB are often time mentioned together and reported to hinder Li diffusion in the cycling, these three defects are intrinsically different and their influence on the electrochemical performance should be viewed separately. Figure 1 shows the schematics comparing these three defects. Figure 1a shows a layered NMC structure without defects, where an ABCABC oxygen stacking sequence presents, known as the O3 phase. In the O3 phase, the LiO$_6$ octahedra share edges with the TMO$_6$ octahedra.[17] However, the ABCABC stacking sequence may be disordered during synthesis or at a highly delithiated state due to layer gliding.[18] These regions with lateral displacements of the layers are SF. Figure 1b gives an example of O1-like SF, where BCBC stacking appears as part of the structure. In this SF region, the LiO$_6$ octahedra and TMO$_6$ octahedra are face-sharing in this SF region. The altered O1 stacking near SF can act as a preferential nucleation site for rocksalt transformation and lead to electrochemical irreversibility.[15,18] This O3 to O1 phase transition leads to the fast capacity decay in NMC materials.[19] Similar behavior was also reported in sodium-ion intercalation compounds as the P2−O2 phase transition and the related poor material durability.[20] In comparison, the ABCABC stacking sequence are well preserved on both sides of the TB or APB, as depicted in Figure 1c,d. Figure 1c shows a crystallographic TB, a plane of lattice points where the grains on two sides of the TB possess mirror symmetry. Figure 1d shows an APB where a translation shift along the c direction separates the structure into two sides. The translation shift causes the Li layer at one side of APB to be continued with the TM layer at the other side of the APB. APB decreases local Li diffusion coefficient and increases cathode impedance because
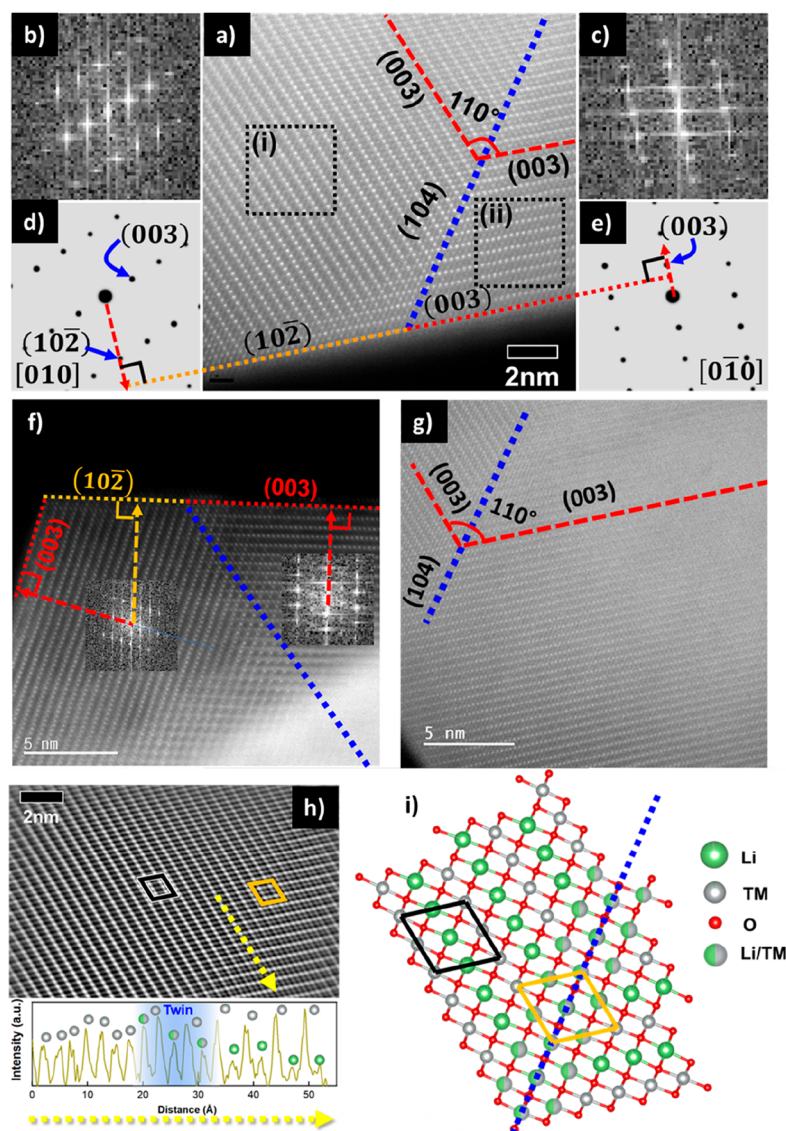
Figure 2. (a) STEM image of a TB-NMC442 particle. The angle between two (003) planes (indicated by red dotted line) divided by the twin boundary (TB, blue dotted line) is 110°. Comparison of Fourier transform patterns from (b) region (i) and (c) region (ii) (as shown on Figure 1a) and simulated diffraction patterns of LiCoO$_2$ with (d) [010] and (e) [0$\bar{1}$0] zone axis. (f) STEM image of a TB-NMC111 particle. (g) STEM image of a TB-NMC622 particle. (h) Fourier filtered image of Figure 1a, which clearly exhibits transition near the TB. (i) Atomic structure near the TB indicated by blue dotted line. Black and orange boxes in (h) and (i) indicate unit cells without and with cation mixing, respectively. Cation disordering is schematically represented as split color circle of Li (green) and TM (gray).

it hinders the Li diffusion pathway along the (003) planes.[21] In comparison, the Li diffusion pathway is still well connected along the two sides of the TB in NMC.

Among the defects discussed above, TB is a unique defect type that does not hinder the Li diffusion and can potentially be beneficial to the electrochemical performance in NMC. In previous literature reports, defects are mostly observed after cycling or exist in a pristine state and then largely increase after cycling. Thus, the generation of defects are usually correlated with the cell performance decay in NMC materials. In this work, however, we report a novel strategy of utilizing highly coherent TB defects to mitigate the structural and performance degradation in NMC particles. The detrimental defects reported in the literature are usually heterogeneous, and the formation of the defects are not well controlled. In contrast, the TB defects reported in this work is introduced to the

pristine material by designing and fabricating through a controlled synthesis, thus functioning as a mitigating strategy in improve the cycling stability of NMC materials.

The designed TB defects in this work are created through a polyol synthesis method in a series of NMC nanoparticles such as LiNi$_{1/3}$Mn$_{1/3}$Co$_{1/3}$O$_2$ (TB-NMC111), LiNi$_{0.4}$Mn$_{0.4}$Co$_{0.2}$O$_2$ (TB-NMC442), and LiNi$_{0.6}$Mn$_{0.2}$Co$_{0.2}$O$_2$ (TB-NMC622). Despite the vast number of studies conducted for layered oxide cathode materials, TB defects have not been reported much in the literature because their presence and abundance heavily depend on the synthesis method to produce the material. For example, in hydroxide coprecipitation, precursors obtained from the reaction are TM hydroxides with a hexagonal ($P\bar{3}m1$) crystal structure. During heat treatment, the precursor will eventually transform into a layered structure ($R\bar{3}m$), but the two structures, hexagonal ($P\bar{3}m1$) and

rhombohedral ($R\bar{3}m$), should be compatible with each other because they both belong to the same trigonal crystal system. This compatibility may reduce the chance to form twins during the phase transition. In contrast, during polyol synthesis, precursors obtained from the initial reaction consist of Ni–Co alloys with a cubic structure.[22] Although they also transform into the layered structure ($R\bar{3}m$) during heat treatment, polyol-synthesized NMC goes through a unique phase transition from cubic ($Fm\bar{3}m$) to rhombohedral ($R\bar{3}m$), which are the structures with much less compatibility. In addition, the phase transformation for polyol synthesis is accompanied by particle size growth from around 5 to 138 nm. It is likely that twins in TB-NMC materials form during this particular phase transformation and particle size growth process.

Using scanning transmission electron microscopy (STEM), we analyzed the crystallographic structure at TBs and the types of surface facets that formed adjacent to the TBs. Our results show that radially aligned TBs observed in TB-NMC materials can maximize the presence of the (003) plane in pristine particles, which is more stable than other planes. Furthermore, the structural changes observed using *operando* XRD verify that TB-NMC442 experiences less *c*-lattice expansion and contraction during charge and discharge. Our results suggest that the rocksalt-like region formed along the TBs can serve as a rigid framework that mitigate the changes in the *c*-lattice during cycling. As a result, TB-NMC materials show enhanced electrochemical performance with better long-term cycling retention compared to commercial NMC samples.

■ RESULTS AND DISCUSSION

Twin Boundary Defects in Pristine TB-NMC. Nanosized TB-NMC111, TB-NMC442, and TB-NMC622 materials are synthesized with a polyol method as described in the Experimental Section. The high-angle annular dark-field (HAADF)-STEM images of the TB-NMC materials are shown in Figure 2. The STEM images are taken along the [010] zone axis and exhibits the bonding of two domains across a (104) plane, forming an atomically sharp boundary that can be universally observed in three NMC materials with different compositions. Each domain has the well-defined layered structure as seen in the literature.[23] The interface, as marked by the blue dotted line in Figure 2a,f,g, was identified as a crystallographic TB. In TB-NMC materials, TB forms in a radial direction, extending from the center to surface of the particle with two (003) planes from the two domains converging to form a 110° angle. Here we want to point out that this 110° angle is related to the intrinsic angle between the (003) and (104) plane in a layered structure, which is 55°. The two (003) planes from the two sides of the (104) plane TB cause the angle between the two (003) planes to add up to 110°, as shown in SI, Figure S1a,b. This 110° angle was also observed in other TB in layered oxide reported previously.[16,24] The symmetry along the TB was further confirmed by Fourier transform (FT) images obtained in two areas (indicated by (i) and (ii) on Figure 2a). The results were compared to the simulated diffraction patterns of LiCoO$_2$ (LCO) with zone axis of [010] and [0$\bar{1}$0] because NMC has the same space group ($R\bar{3}m$) and similar lattice parameters as those of LCO.[25] The FT images in parts b and c of Figure 2 match closely with the simulated diffraction patterns in parts d and e of Figure 2, respectively, confirming the 180° rotational symmetry observed in the STEM image.

Figure 2h: The Fourier-filtered image of Figure 2a more clearly illustrates the atomic structure formed along the TB. At the bottom of this image, the line intensity profile that runs across the TB was collected along the yellow arrow. High and low intensity peaks in the line profile represent the location of TM and Li, respectively; the difference in atomic mass between them leads to Z-contrast. Following the yellow arrow starting on the left domain of the TB, similar intensity peaks are observed at about 2.5 Å spacing because the arrow is on the (003) plane. As the line profile approaches the TB, each alternating peak decreases in intensity as more Li starts to occupy the alternating TM location. Such disordering is gradually alleviated past the TB, where Li and TM are then alternatively arranged on the (10$\bar{2}$) plane. Severe cation disordering observed on the TB and the sites adjacent to it can be viewed as a phase transition, as illustrated by the unit cells denoted by the orange boxes in Figure 2h,i. The atomic structure in the orange box is comparable to the rocksalt structure, as shown in Supporting Information, (SI), Figure S2. This rocksalt-like phase clearly contrasts with the pristine layered structure observed in a unit cell located away from the TB (denoted with a black box in Figure 2h). The cation disorder observed here is different from the cation disorder frequently observed in layered oxide materials (after high-voltage cycling, which is confined to the few atomic layers at the surface of particles).[26] Here, a few atomic layers of the rock-salt like phase are aligned radially, propagating from the center to the surface of the particle along the TBs.

It is important to note that the formation of TBs is a universal phenomenon in classical layered oxides synthesized by the polyol method. The existence of TB has been confirmed by the STEM images from three different TB-NMC compounds (NMC442, NMC111, and NMC622) in Figure 2a,f,g, as well as more particles sharing the same traits in SI, Figure S3, with both high and low-mag STEM images. All of the TBs are formed in the radial direction, and the presence of rocksalt-like phase along the TB are observed. The facet planes near the TB on TB-NMC442 were identified as (10$\bar{2}$) and (003) by their reciprocal vectors on Figure 2d,e (as indicated by red dotted arrows). Other TB-NMC particles in Figure 2f and SI, Figure S3, all provide similar observations, showing that TB-NMC particles are commonly terminated with (10$\bar{2}$) and (003) planes. It is generally accepted that TBs form in the material in order to minimize the total surface energy per volume; studies by Howie and Marks showed that TBs lead to the surface with even lower energy than surfaces developed by the Wulff construction in nanocrystallites.[27−29] Thus, the observed surface facets exposed due to TBs, (10$\bar{2}$) and (003), are low surface energy facets in layered oxide materials. According to a previous report, (003), (104), and (10$\bar{2}$) for LCO (whose crystal structure is identical to NMC) all have a low surface energy of ~1 J/m^2 in contrast to planes such as (110) and (100), which have higher surface energies of 2.41 and 2.943 J/m^2, respectively.[30] The similarities in surface energy values between LCO and NMC are expected due to their structural similarities. A few regions without TBs in NMC442 particles were also observed as shown in SI, Figure S4. Here, without TBs, the particles display facets with high-order planes such as (11$\bar{8}$), (11$\bar{2}$), and (107), which are correlated with higher surface energies.[31] In summary, TB is universally present in polyol synthesized NMC materials. TB-NMC particle surface is more likely terminated with low surface energy planes such as (003) and (10$\bar{2}$) with limited
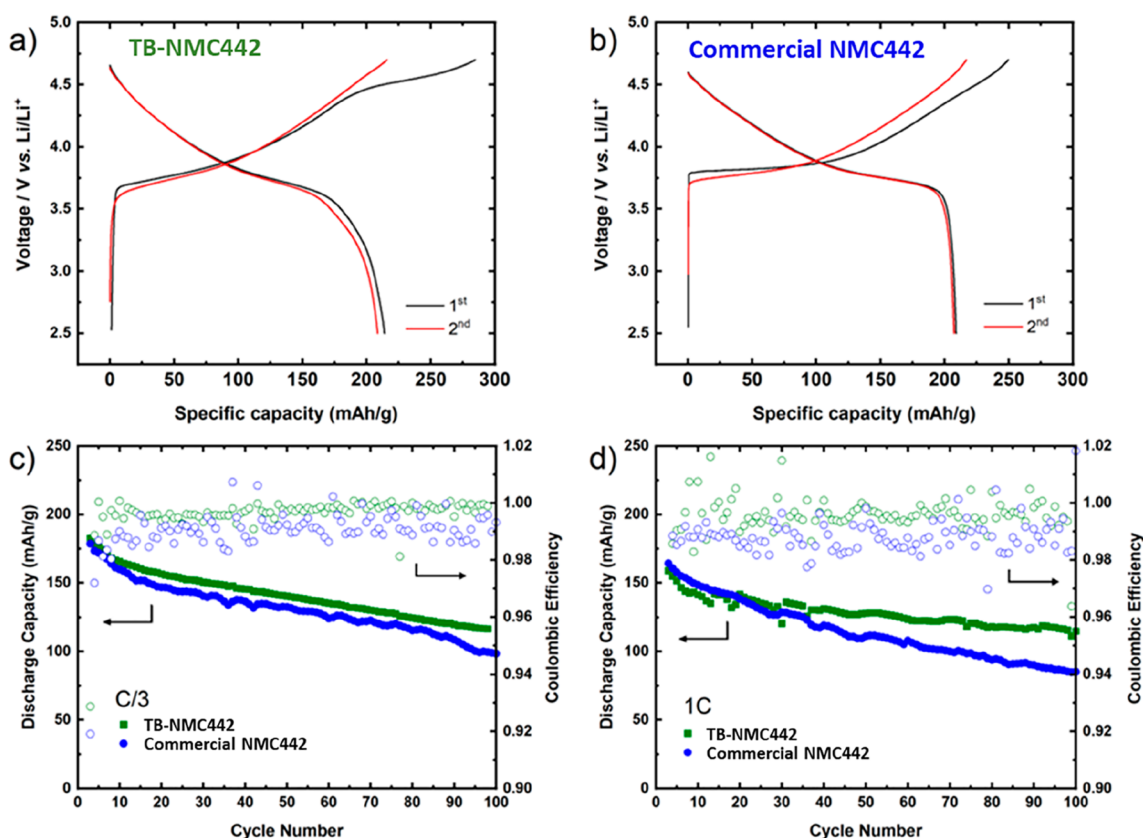
Figure 3. Electrochemical performance of TB-NMC442 and commercial NMC442. (a,b) Respective voltage profile of the first and second cycle and (c,d) respective cycling performance in the voltage range of 2.5−4.7 V.

structural degradation, which will be further discussed in the following sections.

Electrochemical Performance Comparison. To evaluate the performance of the NMC material with the controlled TB defects, TB-NMC442 and a commercially available NMC442 were first tested and compared. SEM images of both samples are shown in SI, Figure S5. TB-NMC442 has a dispersed nanoparticle morphology without agglomeration, while commercial NMC442 consists of tightly packed microsized aggregates. A stable cycling performance of both TB-NMC442 and commercial NMC442 at low voltage cutoff (2.5−4.3 V) and C/10 rate is confirmed in half cell (SI, Figure S6). Commercial NMC442 exhibits slightly higher initial discharge capacity (159.9 mAh g^{-1}) than TB-NMC442 (139.8 mAh g^{-1}), but TB-NMC442 shows higher initial CE (87.9%) than commercial NMC442 (84.1%). After 50 cycles, TB-NMC442 delivers slightly higher capacity retention (87.7%) than commercial NMC442 (86.9%). The two materials do not show significant difference at low voltage cutoff and low rate because less extensive material structure degradation or side reactions with the electrolyte are triggered. Both TB-NMC442 and commercial NMC442 were then tested with a high voltage cutoff (2.5−4.7 V), and the results are shown in Figure 3. Such a high voltage cutoff is used to evaluate the material stability near the completely delithiated state (theoretical capacity ≈ 274 mAh·g^{-1}). As expected, both materials show the typical behavior of layered oxide materials at high voltage cutoffs: high initial capacity but rapid capacity decay with prolonged cycling.[3] Initially, TB-NMC442 has a charge capacity of 284 mAh g^{-1} compared with a capacity of 250 mAh g^{-1} for

commercial NMC442. Because TB-NMC442 is a nanosized material, it has a relatively large surface area of 2.83 m^2 g^{-1}, which is 5 times larger than commercial NMC442 (0.5 m^2 g^{-1}).[32] Thus, more CEI may form in the first cycle and contribute to additional charge capacity in TB-NMC442. SI, Figure S7, shows a comparison of XPS measurements of pristine, electrolyte-soaked, and 10-cycled TB-NMC442 and commercial NMC442. The XPS results further confirm that although the pristine samples look similar, a larger amount CEI is observed for TB-NMC442 after the initial 10 cycles. In addition, a small plateau above 4.5 V in the first charge curve can be observed in TB-NMC442. SI, Figure S8, shows the differential capacity (dQ/dV) curves as a function of voltage. During the first charge, an intense charge peak around 3.8 V can be seen for both samples, but a less-intense peak around 4.5 V is only observed for TB-NMC442. While it is widely acknowledged that the 3.8 V peak corresponds with the oxidation of Ni ions (Ni^{2+}/Ni^{4+}) and Co ions (Co^{3+}/Co^{4+}), the 4.5 V peak is speculated to correlate with oxygen redox or oxygen release from the lattice, previously observed for classical layered oxides[6,33] but notably to a much larger degree in lithium-rich layered oxide materials.[34] It is suspected that a high concentration of TB defects in TB-NMC442 activates a small amount of oxygen redox in the structure which can be induced by the possible Li−O−Li configurations along the TB.[35] In summary, the side reactions with the electrolyte due to the large surface area and the potential activation of oxygen redox or oxygen gas release would contribute to the additional first charge capacity of TB-NMC442, but it remains mainly irreversible as both samples show a similar first discharge
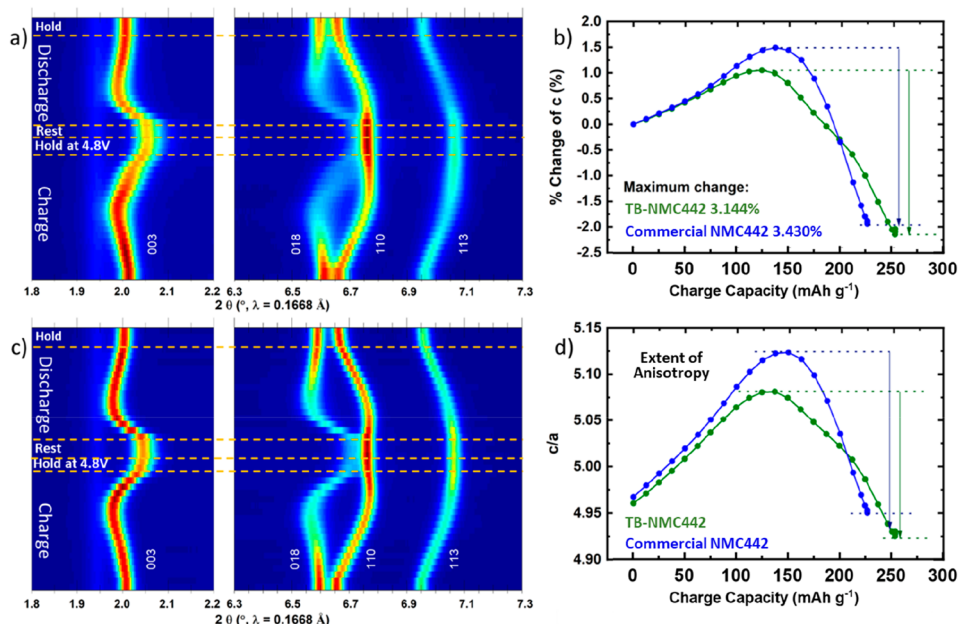
Figure 4. *Operando* X-ray diffraction results of TB-NMC442 and commercial NMC442. Contour plot of the diffraction peak evolution of (003), (018), and (110) planes during the first cycle of (a) TB-NMC442 and (c) commercial NMC442. Comparison of the corresponding calculated lattice parameters along (b) the *c*-axis and (d) the *c*/*a* ratio, showing the degree of anisotropic lattice changes as a function of the specific capacity during charge to 4.8 V (followed by 2 h hold at 4.8 V and rest for 2 h).

capacity (214 mAh g^{-1} for TB-NMC442 and 209 mAh g^{-1} for commercial NMC442).

When both NMCs were repeatedly charged and discharged for a long time with high voltage cutoff, TB-NMC442 shows much improved capacity retention compared to commercial NMC442, especially at high C-rate. After 100 cycles, TB-NMC442 retains a capacity of 116 and 124 mAh g^{-1} at C/3 and 1C rates, respectively, compared to 98 and 85 mAh g^{-1} for commercial NMC442. Moreover, an average efficiency of 99.7% (from the 3rd to the 100th cycle) of TB-NMC442 compared to 99.4% of commercial NMC442 is observed at 1C rate.

The cycling stability improvement is again universally seen in TB containing materials. SI, Figure S9, provides the XRD and SEM for pristine NMC622. Similar to the TB-NMC442 sample, TB-NMC622 are nanoparticles with 50−200 nm grain size, while commercial NMC622 are microsized polycrystalline spherical particles. Rietveld refinement was applied to the XRD pattern for both TB-NMC622 and commercial NMC622, and the detailed parameters are listed in SI, Table S5, showing that both samples have a pure phase which can be well indexed to the $R\bar{3}m$ space group. SI, Figure S10, compares the electrochemical performance for TB-NMC622 and commercial NMC622. At the initial cycle, TB-NMC622 delivers a discharge capacity of 184 mAh g^{-1} and commercial NMC622 delivers a discharge capacity of 186 mAh g^{-1}. After 500 cycles, 14.8−14.9% higher capacity retention is seen in TB-NMC622 compared to commercial NMC622 with both C/3 rate and 1C rate. In addition, an average Coulombic efficiency at 99.0% (from the 3rd to 500th cycle) is observed in TB-NMC622 at 1C rate, compared to 98.7% in commercial NMC622. The electrochemistry data in NMC622 shows that an improved cycling stability is observed in TB-NMC622 compared to commercial NMC622, in phase with the NMC422 data.

Traditionally, it was reported that a high concentration of defects and increased side reactions with the electrolyte adversely affect the electrochemical performance of the material. However, the enhanced electrochemical performance for TB-NMC indicates that there are other factors that need to be considered to depict the full picture. Our hypothesis for improved cycling performance in TB-NMC comes from TB's effects on both the surface reconstruction and the bulk structure evolution. First, as shown in the STEM analysis earlier, radially aligned TBs in TB-NMC442 increase the exposure of surfaces terminated by (003) planes and thus limit the degree of structural degradation on the surface. Surface reconstruction from a layered to a rocksalt-like structure is a common degradation pathway in layered oxides. Studies suggest that more severe reconstruction is observed from surfaces terminated with non-(003) planes or when Li diffusion channels are exposed to the electrolyte.[3,36] The degree of reconstruction on the surfaces terminated by the (003) plane, on the other hand, are much more limited (only 2−3 atomic layers). Our study is consistent with such expectations that minimal surface reconstruction was observed for cycled TB-NMC442 samples.[22] Furthermore, TBs in TB-NMC442 can affect bulk structural evolution, as discussed in more detail in the following section.

Structural and Morphological Evolution in TB-Containing NMC. Synchrotron XRD (sXRD) and Rietveld refinement was performed on both TB-NMC442 and commercial NMC442 electrodes, as shown in SI, Figure S5. For both samples, all peaks can be indexed to the α-NaFeO$_2$-type structure (with $R\bar{3}m$ space group) or to the PTFE binder additive. The results from Rietveld refinement are tabulated in SI, Table S4. The refined lattice parameters of TB-NMC442 have slightly smaller *a* and *c* lattice parameters, *a* of 2.86868(4) Å and *c* of 14.2304(3) Å, compared to *a* of 2.87265(2) Å and *c* of 14.2692(1) Å in commercial NMC442. A slightly larger degree of Li/Ni mixing of 5.66(8)% for TB-NMC442 was also
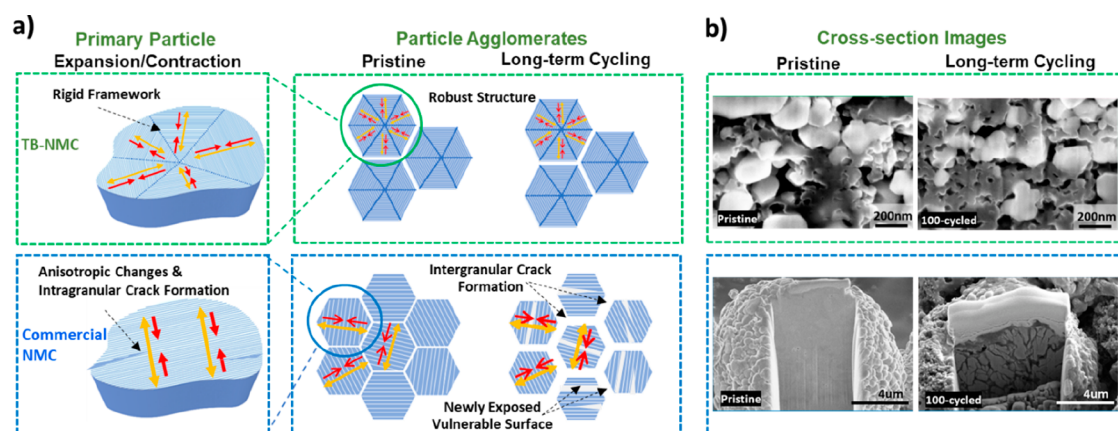
Figure 5. (a) Schematic of the proposed mechanism showing how TBs can alleviate *c*-lattice changes during cycling and mitigate intragranular and intergranular crack formation in NMC materials. (b) Cross sectional images of pristine and 100-cycled TB-NMC442 (green frames) and commercial NMC442 (blue frames).

observed compared to the 5.10(5)% of commercial NMC442. After the characterization of the pristine states, both NMC samples were charged to 4.8 V and discharged to 2.7 V with *operando* sXRD, as shown in SI, Figure S11. Parts a and c of Figure 4 are 2D image plots of the 003 and 110 reflections during the first charge−discharge cycle, which are strong indications for the lattice changes occurring along the *c*- and *a*-directions, respectively. Consistent with previous studies of other layered oxides,[37] the (003) peak shifts to higher angles during charge as oxygen atoms in TM layer repulse with one another after Li diffuses out of the structure. Meanwhile, the *a*-lattice contracts at a high state of charge, consistent with other low-Ni content NMCs observed in the literature.[37]

Parts b and d of Figure 4 and SI, Figure S12, represent the relative changes in the refined lattice parameters and the total volume (obtained from LeBail refinements) as a function of the specific capacity obtained from the electrochemistry data for both NMC442 materials. The absolute values for the lattice parameters along charge and discharge are also available in Figure S11. The lattice parameters are also plotted with respect to the voltage (in SI, Figure S13), compared to plotting versus specific capacity in Figure 4b,d, and SI, Figure S12. Nonetheless, both results confirm that TB-NMC442 experiences less relative *c*-lattice expansion and contraction during the charge and discharge process even though both samples have identical composition (as confirmed by ICP result in SI, Table S2). When comparing the total percentage of the *c* lattice parameter change during charge (i.e., from peak to trough), TB-NMC442 experiences a 3.14% change compared to the 3.43% change experienced by commercial NMC442. Here we want to emphasize that, in principle, the commercial NMC442 should have much smaller *c* lattice change because the obtained capacity is smaller than TB-NMC442. However, the observed opposite trend that commercial NMC442 shows larger *c* lattice change clearly show that the TB in NMC can mitigate the anisotropic changes.

Repeated anisotropic changes (expansion in *c*, contraction in *a*)[37−39] causes strain in lattice dimensions during Li extraction and insertion, which has been generally considered to be the major cause of particle cracking in the layered oxide materials. Such cracks are widely suspected to contribute to NMC degradation at high voltage. The cracks weaken the connections between materials and cause increased impedance as well as reduced electrochemical contact.[40] Furthermore,

they allow electrolyte penetration into the interior of the cycled particles, which leads to severe parasitic reactions and irreversible phase transformation.[41,42] In our sXRD refinement results, the reduced *c* lattice expansion results in smaller anisotropic changes for TB-NMC442, indicating that TB-NMC442 is subjected to much less strain (Figure 4d and SI, Figure S13b) during cycling, thus showing an improved high voltage cycling stability.

On the basis of the results above, Figure 5a presents a schematic of the proposed mechanism showing how TBs can alleviate *c*-lattice changes, mitigate intragranular and inter-granular crack formation, and improve cycling stability for NMC materials. In commercial NMC, the primary particles experience expansion and contraction during cycling, especially along the *c*-direction. Intragranular cracks are easily formed and propagate during long-term cycling with the continuous *c*-lattice changes, as suggested by STEM images of cycled NMC particles in many previous reports.[43,44] In this work, such intragranular cracks were also captured by HR-TEM images of 500-cycled commercial NMC622, as shown in SI, Figure S14a. During long-term cycling, the primary particles could eventually break, and intergranular cracks can also form in the densely packed secondary particles as a result of continuous primary particle expansion/contraction. Severe intergranular cracks are observed in commercial NMC442 after cycling, shown in Figure 5b. The intragranular and intergranular crack formation will lead to the exposure of additional surfaces where parasitic reactions with the electro-lyte will occur, resulting in the increase of electrical resistivity by disconnecting the charge transport pathway in the electrode. This will contribute to the capacity degradation in commercial NMC as cycling proceeds, as previously shown in Figure 3 and SI, Figure S10. It is important to note that the facets that are newly exposed during both intragranular and intergranular cracking may be more vulnerable to reacting with the electrolyte compared to the original surface facets of the secondary particles in commercial NMC. This comes from the differences in the formation of the interior and exterior primary particles during synthesis. While the exterior particles form surface facets with the minimized surface energy, interior particles form surface facets with minimized grain boundary energy. Grain boundary energy is decided by the relative crystallographic orientation between the neighboring primary particles. A lower misorientation angle generally leads to lower

grain boundary energy. However, the minimization of the misorientation angle (and the lower grain boundary energy) does not guarantee lower surface energies. Thus, it is expected that the surface of newly exposed interior particles is more likely terminated by non-(003) planes.[45] The non-(003) planes in the newly exposed particles are subjected to more vulnerability to side reactions. Thus, a combination of increased surface area and increased vulnerability will accelerate the capacity degradation of commercial NMC. In the HR-TEM images of cycled commercial NMC622 shown in SI, Figure S14b, clear surface rocksalt phase transformation was observed, indicating the poor surface stability of commercial NMC622 samples.

In comparison, the benefit of having the designed TB in NMC mainly comes from two aspects: (1) pristine TB-NMC particles are mostly terminated with more stable planes as suggested by Figure 2 and SI, Figure S3, preventing the parasitic side reactions between cathode and electrolyte. The surface stability of TB-NMC is evaluated with HR-TEM (SI, Figure S14c,S14d), where the layered structure was well maintained after 500 cycles and no intragranular cracking was observed. (2) In long-term cycling, the existence of TB alleviates the intragranular crack formation and new surface exposure to the electrolyte, as illustrated in Figure 5a. In TB-NMC, the radially aligned TBs and the rocksalt-like phase formed along the TBs act as a rigid framework that does not expand and contract during cycling. This rigid framework in TB-NMC leads to a relative robust structure compared to commercial NMC, alleviating anisotropic changes and intragranular crack formation. Note that this alleviation effect does not necessarily require multiple TBs presenting in one grain. Even just one TB along the particle would mitigate the changes in c lattice, as suggested by SI, Figure S15. In addition, it is expected that TB-NMC442 has higher fracture toughness due to its smaller particle size. Previous studies have shown that layered oxide materials have a critical particle size below which crack formation can be prevented during cycling.[46,47] The critical particle size is about 200 nm for $LiNi_{1/3}Mn_{1/3}Co_{1/3}O_2$ and 80 nm for $LiNi_{0.80}Co_{0.15}Al_{0.05}O_2$,[47] comparable to the particle size of TB-NMC442 (138 nm).[22] Thus, the robust structure and the higher fracture toughness in TB-NMC mitigates the formation of intragranular and intergranular cracks. Consistent with these hypotheses, Figure 5b and SI, Figure S16, show two contrasting morphological trends observed for TB-NMC442 and commercial NMC442. While almost no change in morphology is observed in TB-NMC442, but severe microcracks are observed in commercial NMC442 after 100 cycles. Similar morphology comparison in TB-NMC622 and commercial NMC622 after 500 cycles is shown in SI, Figure S17, where severe intergranular cracks are seen in commercial NMC622.

CONCLUSIONS

In this work, TB defects are designed and introduced to NMC oxide materials through the polyol synthesis method. The existence of the radially aligned TB defects is confirmed through high resolution STEM in a series of layered NMC materials. Compared to commercially available NMC samples, multiple TB-NMC materials show an improved cycling stability at high voltage and high rate. For TB-NMC442 cycled at the 1C rate between 2.5 and 4.7 V, it shows 17.3% more capacity retention compared to commercial NMC442 after 100 cycles. For TB-NMC622 with the same voltage cutoff

and rate, it also shows 13.8% more capacity retention compared to commercial NMC622 after 500 cycles. An atomic scale analysis of the TB defects and its relationship with the enhanced electrochemical performance is presented in this study with advanced characterization tools. Two beneficial features of the designed TB defects are deconvoluted: First, TB-NMC particles are mostly terminated with the (003) plane, which is a more stable surface against the electrolyte. Thus, TB-NMC prevents the parasitic side reactions between NMC cathode and electrolyte during cycling. Second, a rocksalt-like phase formed along the TBs can act as a rigid framework that mitigates the anisotropic changes and intragranular crack formation during cycling. In TB-NMC, the increased surface stability and high fracture toughness originated from the designed TB defects can effectively mitigate the structural degradation and capacity fade in NMC materials. This work sheds light on defect engineering as a novel and universal strategy for the future design of cathode materials for high voltage LIBs with ultralong cycling life.

EXPERIMENTAL METHODS

Electrochemistry. Synthesis of TB-NMC nanoparticles was carried out following a procedure detailed in a previous study.[22] Using tetraethylene glycol (Aldrich) solvent, all the transition metal acetates, $(NiCH_3COO)_2 \cdot 4H_2O$ (Acros), $(MnCH_3COO)_2 \cdot 4H_2O$ (Acros), and $(CoCH_3COO)_2 \cdot 4H_2O$ (Acros), and $LiOH \cdot H_2O$ (Sigma-Aldrich) were mixed with citric acid (Sigma-Aldrich). All the salt precursors were dissolved when the mixture was heated to 230 °C for 3 h in a round-bottom flask connected to a reflux. Once the mixture cooled down to room temperature, the precipitate was washed with ethanol, dried overnight, and heat-treated at 450 °C for 12 h in air. The powder was then ground with an agate mortar and pestle, pelletized, and then heat treated at 850 °C for 5 h in air. Commercial NMC442 and commercial NMC622 (Toda) powder was heated to 500 °C in air to remove proton-containing surface species.[48] All of the NMC powders were stored in an Ar-filled glovebox (MBraun, <1 ppm of H_2O). SI, Table S1, summarizes the coin cell configuration used for our study. For both TEM and FIB characterization, all cells were cycled at a rate of C/10. For long-term electrochemical results, C/10 was used for the first two formation cycles, while a rate of 1C or C/3 was used for subsequent cycles. Cycling was performed in the voltage range of 2.5−4.7 V with the theoretical capacity defined as 200 mAh g^{-1}. The galvanostatic cycling tests were conducted with an Arbin BT2000 cycler (Arbin instruments, USA).

Material Characterization (TEM, FIB, SEM, XPS, ICP, XRD). High-resolution STEM images for NMC442 and NMC111 materials were taken using the double aberration-corrected scanning TEM (TEAM 0.5) at the Molecular Foundry at Lawrence Berkeley National Laboratory. The STEM was operated at an acceleration voltage of 300 kV. All annular dark-field STEM micrographs were recorded with a convergence angle of 30 mrad and a probe size of <1 Å after fine-tuning of the probe corrector at 300 kV. High-resolution STEM images for 622 material was performed on JEOL JEM-ARM300CF at 300 kV, equipped with spherical aberration correctors. The morphologies of the particles were identified using a Zeiss Sigma 500 scanning electron microscope (SEM) with an accelerating voltage of 5 kV. Cross-sectional images of commercial NMC were collected from focused ion beam (FIB) using the FEI Scios DualBeam FIB. The chemical composition of NMC materials were confirmed by ICP-MS (iCAP RQ, ThermoFisher Scientific) and listed in SI, Table S2 and S3. X-ray photoelectron spectroscopy (XPS) was performed using a Kratos AXIS Supra with an Al anode source operated at 15 kV. High-resolution spectra were calibrated using the hydrocarbon C 1s peak at 284.5 eV. Lab-based X-ray diffraction (XRD) was collected on Rigaku SmartLab Diffractometer with Cu Kα source. *Operando* XRD experimental details will be shared in the following section.

***Operando* X-ray Diffraction.** Electrode pellets were prepared by mixing the NMC powders with carbon black (Timcal Super C65) and polytetrafluoroethylene (PTFE) powder (Sigma-Aldrich, 1 μm particle size), in a 7:1:2 weight ratio. Approximately 6 mg of the mixture was pressed in a 3 mm diameter die to form ~400 μm-thick pellets. The NMC electrode pellets were assembled into modified RATIX electrochemical cells[49] by using lithium foil (MTI Corp) as a counter electrode and two layers of glass fiber (Whatman GF/B) as the separator. The electrolyte used was 1 M $LiPF_6$ dissolved in a mixture of ethylene carbonate (EC) and dimethyl carbonate (DMC) in a 1:1 volume ratio (Sigma-Aldrich). All preparations were carried out in an argon-filled glovebox containing <1 ppm of O_2 and H_2O. Electrochemical measurements were carried out at a rate of 18.58 mA g^{-1} of NMC between 4.8 and 2.7 V, with a 2 h potentiostatic hold at each voltage limit followed by a 2 h rest period (Biologic BCS-810).

Operando synchrotron X-ray diffraction data were recorded during electrochemical measurements using high-energy X-rays (λ = 0.1668 Å) provided by beamline 28-ID-1 at the National Synchrotron Light Source II (NSLS-II) at Brookhaven National Laboratory. Each diffraction image was obtained from a 30 s summed exposure recorded in transmission geometry as the electrode was scanned horizontally in transverse mode, gauging the whole diameter of the electrode. XRD patterns were obtained from integration of the images using the GSAS-II software[50] and using LaB$_6$ (NIST SRM 660c) as a standard for calibration.

XRD Refinements. Rietveld refinements to the XRD data (pristine state) were performed with Topas-Academic V6 using a model based on the $R\bar{3}m$ space group, with TM site (3a) and O site (6c) occupancy based on the nominal composition, and Li site (3b) occupancy based on the electrochemical data. Refined parameters included lattice parameters (a, c), Li−Ni antisite mixing (3a−3b site exchange), O z coordinate, scale factor, isotropic atomic displacement parameters (B_{iso}) for TM and O (fixed to 1 Å^2 for Li). Background and additional peaks from the glass tube container and PTFE additive were fit using a six-coefficient Chebyshev polynomial function and a pseudo-Voigt function, respectively. The lattice parameters during cycling were obtained from LeBail refinements using the $R\bar{3}m$ space group and the same peak profile function as the one used for the Rietveld refinement. The refined parameters for pristine NMC442 and NMC622 samples are shown in SI, Tables S4 and S5.

■ ASSOCIATED CONTENT

ⓈＩ Supporting Information

The Supporting Information is available free of charge at https://pubs.acs.org/doi/10.1021/acs.chemmater.2c01234.

> More STEM images of pristine TB-NMC and commercial NMC particles; XRD and SEM of NMC622 and NMC442 samples; CV and cycling performance comparison between TB-NMC and commercial NMC particles; detailed sXRD refinement results of NMC442 samples; HR-TEM of cycled NMC materials; cross-section images of NMC442 and NMC622 samples before and after cycling; cell assembling details; ICP results (PDF)

■ AUTHOR INFORMATION

Corresponding Authors

  Y. Shirley Meng − *Department of NanoEngineering, University of California San Diego, La Jolla, California 92093, United States; Pritzker School of Molecular Engineering, The University of Chicago, Chicago, Illinois 60637, United States;* ⓞ orcid.org/0000-0001-8936-8845; Email: shirleymeng@uchicago.edu

  Minghao Zhang − *Department of NanoEngineering, University of California San Diego, La Jolla, California 92093, United States;* Email: miz016@eng.ucsd.edu

  Suk Jun Kim − *School of Energy, Materials and Chemical Engineering, Korea University of Technology and Education, Cheonan 31253, Republic of Korea;* Email: skim@koreatech.ac.kr

Authors

  Hyeseung Chung − *Department of NanoEngineering, University of California San Diego, La Jolla, California 92093, United States*

  Yixuan Li − *Department of NanoEngineering, University of California San Diego, La Jolla, California 92093, United States*

  Antonin Grenier − *Department of Chemistry, Stony Brook University, Stony Brook, New York 11794, United States*

  Carlos Mejia − *Department of NanoEngineering, University of California San Diego, La Jolla, California 92093, United States*

  Diyi Cheng − *Department of NanoEngineering, University of California San Diego, La Jolla, California 92093, United States;* ⓞ orcid.org/0000-0003-1616-9209

  Baharak Sayahpour − *Department of NanoEngineering, University of California San Diego, La Jolla, California 92093, United States*

  Chengyu Song − *National Center for Electron Microscopy, Molecular Foundry, Lawrence Berkeley National Laboratory, Berkeley, California 94720, United States*

  Meghan Hannah Shen − *Department of NanoEngineering, University of California San Diego, La Jolla, California 92093, United States;* ⓞ orcid.org/0000-0002-0447-0160

  Ricky Huang − *Department of NanoEngineering, University of California San Diego, La Jolla, California 92093, United States*

  Erik A. Wu − *Department of NanoEngineering, University of California San Diego, La Jolla, California 92093, United States*

  Karena W. Chapman − *Department of Chemistry, Stony Brook University, Stony Brook, New York 11794, United States;* ⓞ orcid.org/0000-0002-8725-5633

Complete contact information is available at: https://pubs.acs.org/10.1021/acs.chemmater.2c01234

Author Contributions

H.C., Y.L., and M.Z. contributed equally to the work. H.C., Y.L., M.Z., S.J.K., and Y.S.M. designed the experiments. H.C., S.J.K., M.Z., and C.S. conducted STEM testing and data analysis. Y.L. and H.C. conducted material synthesis, electrochemistry testing, ICP, SEM, XPS, and XRD analysis. A.G. and K.W.C. conducted operando XRD tests. B.S. conducted lab XRD tests. B.S. and D.C. conducted FIB and SEM test. C.M., M.H.S., and R.H. contributed to material synthesis. E.A.W. conducted XPS tests. M.Z., S.J.K., and Y.S.M. supervised the research. Y.L. and H.C. wrote the manuscript. All authors contributed to the discussion and provided feedback on the manuscript.

Notes

The authors declare no competing financial interest.

■ ACKNOWLEDGMENTS

■ REFERENCES

(1) Liu, Y.; Harlow, J.; Dahn, J. Microstructural Observations of "Single Crystal" Positive Electrode Materials Before and After Long Term Cycling by Cross-Section Scanning Electron Microscopy. *J. Electrochem. Soc.* **2020**, *167* (2), 020512.

(2) Harlow, J. E.; Ma, X.; Li, J.; Logan, E.; Liu, Y.; Zhang, N.; Ma, L.; Glazier, S. L.; Cormier, M. M. E.; Genovese, M.; Buteau, S.; Cameron, A.; Stark, J. E.; Dahn, J. R. A Wide Range of Testing Results on an Excellent Lithium-Ion Cell Chemistry to Be Used as Benchmarks for New Battery Technologies. *J. Electrochem. Soc.* **2019**, *166* (13), A3031−A3044.

(3) Lin, F.; Markus, I. M.; Nordlund, D.; Weng, T. C.; Asta, M. D.; Xin, H. L.; Doeff, M. M. Surface Reconstruction and Chemical Evolution of Stoichiometric Layered Cathode Materials for Lithium-Ion Batteries. *Nat. Commun.* **2014**, *5*, 3529.

(4) Dixit, M.; Markovsky, B.; Schipper, F.; Aurbach, D.; Major, D. T. Origin of Structural Degradation during Cycling and Low Thermal Stability of Ni-Rich Layered Transition Metal-Based Electrode Materials. *J. Phys. Chem. C* **2017**, *121* (41), 22628−22636.

(5) Sharifi-Asl, S.; Lu, J.; Amine, K.; Shahbazian-Yassar, R. Oxygen Release Degradation in Li-Ion Battery Cathode Materials: Mechanisms and Mitigating Approaches. *Adv. Energy Mater.* **2019**, *9* (22), 1900551.

(6) Jung, R.; Metzger, M.; Maglia, F.; Stinner, C.; Gasteiger, H. A. Oxygen Release and Its Effect on the Cycling Stability of LiNi x Mn y Co z O 2 (NMC) Cathode Materials for Li-Ion Batteries. *J. Electrochem. Soc.* **2017**, *164* (7), A1361−A1377.

(7) Zhan, C.; Wu, T.; Lu, J.; Amine, K. Dissolution, Migration, and Deposition of Transition Metal Ions in Li-Ion Batteries Exemplified by Mn-Based Cathodes − a Critical Review. *Energy Environ. Sci.* **2018**, *11* (2), 243−257.

(8) Asenbauer, J.; Eisenmann, T.; Kuenzel, M.; Kazzazi, A.; Chen, Z.; Bresser, D. The Success Story of Graphite as a Lithium-Ion Anode Material − Fundamentals, Remaining Challenges, and Recent Developments Including Silicon (Oxide) Composites. *Sustainable Energy & Fuels* **2020**, *4* (11), 5387−5416.

(9) De Biasi, L.; Schwarz, B.; Brezesinski, T.; Hartmann, P.; Janek, J.; Ehrenberg, H. Chemical, Structural, and Electronic Aspects of Formation and Degradation Behavior on Different Length Scales of Ni-Rich NCM and Li-Rich HE-NCM Cathode Materials in Li-Ion Batteries. *Adv. Mater.* **2019**, *31* (26), 1900985.

(10) Ryu, H. H.; Park, K. J.; Yoon, C. S.; Sun, Y. K. Capacity Fading of Ni-Rich Li[NixCoyMn1-x-y]O2 (0.6 ≤ x ≤ 0.95) Cathodes for High-Energy-Density Lithium-Ion Batteries: Bulk or Surface Degradation? *Chem. Mater.* **2018**, *30* (3), 1155−1163.

(11) Lee, E. J.; Chen, Z.; Noh, H. J.; Nam, S. C.; Kang, S.; Kim, D. H.; Amine, K.; Sun, Y. K. Development of Microstrain in Aged Lithium Transition Metal Oxides. *Nano Lett.* **2014**, *14* (8), 4873−4880.

(12) Kim, J. H.; Park, K. J.; Kim, S. J.; Yoon, C. S.; Sun, Y. K. A Method of Increasing the Energy Density of Layered Ni-Rich Li[Ni 1−2: X Co x Mn x]O 2 Cathodes (x = 0.05, 0.1, 0.2). *Journal of Materials Chemistry A* **2019**, *7* (6), 2694−2701.

(13) Zhang, S. S. Problems and Their Origins of Ni-Rich Layered Oxide Cathode Materials. *Energy Storage Materials* **2020**, *24*, 247−254.

(14) Singer, A.; Zhang, M.; Hy, S.; Cela, D.; Fang, C.; Wynn, T. A.; Qiu, B.; Xia, Y.; Liu, Z.; Ulvestad, A.; Hua, N.; Wingert, J.; Liu, H.; Sprung, M.; Zozulya, A. v.; Maxey, E.; Harder, R.; Meng, Y. S.; Shpyrko, O. G. Nucleation of Dislocations and Their Dynamics in Layered Oxide Cathode Materials during Battery Charging. *Nature Energy* **2018**, *3* (8), 641−647.

(15) Han, M.; Liu, Z.; Shen, X.; Yang, L.; Shen, X.; Zhang, Q.; Liu, X.; Wang, J.; Lin, H.; Chen, C.; Pao, C.; Chen, J.; Kong, Q.; Yu, X.; Yu, R.; Gu, L.; Hu, Z.; Wang, X.; Wang, Z.; Chen, L. Stacking Faults Hinder Lithium Insertion in Li 2 RuO 3. *Adv. Energy Mater.* **2020**, *10* (48), 2002631.

(16) Li, S.; Yao, Z.; Zheng, J.; Fu, M.; Cen, J.; Hwang, S.; Jin, H.; Orlov, A.; Gu, L.; Wang, S.; Chen, Z.; Su, D. Direct Observation of Defect-Aided Structural Evolution in a Nickel-Rich Layered Cathode. *Angew. Chem.* **2020**, *132* (49), 22276−22283.

(17) Van der Ven, A.; Aydinol, M. K.; Ceder, G.; Kresse, G.; Hafner, J. First-Principles Investigation of Phase Stability in LixCoO2. *Phys. Rev. B* **1998**, *58* (6), 2975−2987.

(18) Wang, C.; Han, L.; Zhang, R.; Cheng, H.; Mu, L.; Kisslinger, K.; Zou, P.; Ren, Y.; Cao, P.; Lin, F.; Xin, H. L. Resolving Atomic-Scale Phase Transformation and Oxygen Loss Mechanism in Ultrahigh-Nickel Layered Cathodes for Cobalt-Free Lithium-Ion Batteries. *Matter* **2021**, *4*, 2013−2026.

(19) Robert, R.; Villevieille, C.; Novák, P. Enhancement of the High Potential Specific Charge in Layered Electrode Materials for Lithium-Ion Batteries. *Journal of Materials Chemistry A* **2014**, *2* (23), 8589.

(20) Huang, J. J.; Weinstock, D.; Hirsh, H.; Bouck, R.; Zhang, M.; Gorobtsov, O. Yu.; Okamura, M.; Harder, R.; Cha, W.; Ruff, J. P. C.; Meng, Y. S.; Singer, A. Disorder Dynamics in Battery Nanoparticles During Phase Transitions Revealed by Operando Single-Particle Diffraction. *Adv. Energy Mater.* **2022**, *12* (12), 2103521.

(21) Ahmed, S.; Pokle, A.; Bianchini, M.; Schweidler, S.; Beyer, A.; Brezesinski, T.; Janek, J.; Volz, K. Understanding the Formation of Antiphase Boundaries in Layered Oxide Cathode Materials and Their Evolution upon Electrochemical Cycling. *Matter* **2021**, *4* (12), 3953−3966.

(22) Chung, H.; Grenier, A.; Huang, R.; Wang, X.; Lebens-Higgins, Z.; Doux, J. M.; Sallis, S.; Song, C.; Ercius, P.; Chapman, K.; Piper, L. F. J.; Cho, H. M.; Zhang, M.; Meng, Y. S. Comprehensive Study of a Versatile Polyol Synthesis Approach for Cathode Materials for Li-Ion Batteries. *Nano Research* **2019**, *12* (9), 2238−2249.

(23) Lin, F.; Markus, I. M.; Nordlund, D.; Weng, T. C.; Asta, M. D.; Xin, H. L.; Doeff, M. M. Surface Reconstruction and Chemical Evolution of Stoichiometric Layered Cathode Materials for Lithium-Ion Batteries. *Nat. Commun.* **2014**, *5*, 3529.

(24) Jiang, Y.; Yan, P.; Yu, M.; Li, J.; Jiao, H.; Zhou, B.; Sui, M. Atomistic Mechanism of Cracking Degradation at Twin Boundary of LiCoO2. *Nano Energy* **2020**, *78*, 105364.

(25) Moriwake, H.; Kuwabara, A.; Fisher, C. A. J.; Huang, R.; Hitosugi, T.; Ikuhara, Y. H.; Oki, H.; Ikuhara, Y. First-Principles Calculations of Lithium-Ion Migration at a Coherent Grain Boundary in a Cathode Material, LiCoO2. *Adv. Mater.* **2013**, 25 (4), 618−622.

(26) Zheng, J.; Yan, P.; Zhang, J.; Engelhard, M. H.; Zhu, Z.; Polzin, B. J.; Trask, S.; Xiao, J.; Wang, C.; Zhang, J. Suppressed Oxygen Extraction and Degradation of LiNixMnyCozO2cathodes at High Charge Cut-off Voltages. *Nano Research* **2017**, 10 (12), 4221−4231.

(27) Wulff, G. XXV. Zur Frage Der Geschwindigkeit Des Wachsthums Und Der Auflösung Der Krystallflächen. *Zeitschrift für Kristallographie - Crystalline Materials* **1901**, 34 (1), 449−530.

(28) Marks, L. D. Surface Structure and Energetics of Multiply Twinned Particles. *Philosophical Magazine A* **1984**, 49 (1), 81−93.

(29) Howie, A.; Marks, L. D. Elastic Strains and the Energy Balance for Multiply Twinned Particles. *Philosophical Magazine A* **1984**, 49 (1), 95−109.

(30) Kramer, D.; Ceder, G. Tailoring the Morphology of LiCoO2: A First Principles Study. *Chem. Mater.* **2009**, 21 (16), 3799−3809.

(31) Howe, J. M. *Interfaces in Materials*, 1st ed.; Wiley-Interscience: New York, 1997.

(32) Chung, H.; Grenier, A.; Huang, R.; Wang, X.; Lebens-Higgins, Z.; Doux, J. M.; Sallis, S.; Song, C.; Ercius, P.; Chapman, K.; Piper, L. F. J.; Cho, H. M.; Zhang, M.; Meng, Y. S. Comprehensive Study of a Versatile Polyol Synthesis Approach for Cathode Materials for Li-Ion Batteries. *Nano Research* **2019**, 12 (9), 2238−2249.

(33) Li, J.; Petibon, R.; Glazier, S.; Sharma, N.; Pang, W. K.; Peterson, V. K.; Dahn, J. R. In-Situ Neutron Diffraction Study of a High Voltage Li(Ni0.42Mn0.42Co0.16)O2/Graphite Pouch Cell. *Electrochim. Acta* **2015**, 180, 234−240.

(34) Teufl, T.; Strehle, B.; Müller, P.; Gasteiger, H. A.; Mendez, M. A. Oxygen Release and Surface Degradation of Li- and Mn-Rich Layered Oxides in Variation of the Li 2 MnO 3 Content. *J. Electrochem. Soc.* **2018**, 165 (11), A2718−A2731.

(35) Seo, D.-H.; Lee, J.; Urban, A.; Malik, R.; Kang, S.; Ceder, G. The Structural and Chemical Origin of the Oxygen Redox Activity in Layered and Cation-Disordered Li-Excess Cathode Materials. *Nat. Chem.* **2016**, 8 (7), 692−697.

(36) Zhang, F.; Lou, S.; Li, S.; Yu, Z.; Liu, Q.; Dai, A.; Cao, C.; Toney, M. F.; Ge, M.; Xiao, X.; Lee, W. K.; Yao, Y.; Deng, J.; Liu, T.; Tang, Y.; Yin, G.; Lu, J.; Su, D.; Wang, J. Surface Regulation Enables High Stability of Single-Crystal Lithium-Ion Cathodes at High Voltage. *Nat. Commun.* **2020**, 11, 3050.

(37) Li, W.; Asl, H. Y.; Xie, Q.; Manthiram, A. Collapse of LiNi1- x-YCoxMnyO2 Lattice at Deep Charge Irrespective of Nickel Content in Lithium-Ion Batteries. *J. Am. Chem. Soc.* **2019**, 141 (13), 5097−5101.

(38) Chen, J.; Yang, H.; Li, T.; Liu, C.; Tong, H.; Chen, J.; Liu, Z.; Xia, L.; Chen, Z.; Duan, J.; Li, L. The Effects of Reversibility of H2-H3 Phase Transition on Ni-Rich Layered Oxide Cathode for High-Energy Lithium-Ion Batteries. *Front. Chem.* **2019**, 7, 500.

(39) Xu, X.; Huo, H.; Jian, J.; Wang, L.; Zhu, H.; Xu, S.; He, X.; Yin, G.; Du, C.; Sun, X. Radially Oriented Single-Crystal Primary Nanosheets Enable Ultrahigh Rate and Cycling Properties of LiNi 0.8 Co 0.1 Mn 0.1 O 2 Cathode Material for Lithium-Ion Batteries. *Adv. Energy Mater.* **2019**, 9, 1803963.

(40) Hu, J.; Li, L.; Hu, E.; Chae, S.; Jia, H.; Liu, T.; Wu, B.; Bi, Y.; Amine, K.; Wang, C.; Zhang, J.; Tao, J.; Xiao, J. Mesoscale-Architecture-Based Crack Evolution Dictating Cycling Stability of Advanced Lithium Ion Batteries. *Nano Energy* **2021**, 79, 105420.

(41) Li, H.; Liu, A.; Zhang, N.; Wang, Y.; Yin, S.; Wu, H.; Dahn, J. R. An Unavoidable Challenge for Ni-Rich Positive Electrode Materials for Lithium-Ion Batteries. *Chem. Mater.* **2019**, 31 (18), 7574−7583.

(42) Zhao, W.; Zou, L.; Jia, H.; Zheng, J.; Wang, D.; Song, J.; Hong, C.; Liu, R.; Xu, W.; Yang, Y.; Xiao, J.; Wang, C.; Zhang, J.-G. Optimized Al Doping Improves Both Interphase Stability and Bulk Structural Integrity of Ni-Rich NMC Cathode Materials. *ACS Applied Energy Materials* **2020**, 3 (4), 3369−3377.

(43) Yan, P.; Zheng, J.; Gu, M.; Xiao, J.; Zhang, J.-G.; Wang, C.-M. Intragranular Cracking as a Critical Barrier for High-Voltage Usage of Layer-Structured Cathode for Lithium-Ion Batteries. *Nat. Commun.* **2017**, 8, 14101.

(44) Wei, W.; Ding, Z.; Chen, C.; Yang, C.; Han, B.; Xiao, L.; Liang, C.; Gao, P.; Cho, K. Surface-Dependent Stress-Corrosion Cracking in Ni-Rich Layered Oxide Cathodes. *Acta Mater.* **2021**, 212, 116914.

(45) Kim, J. H.; Kim, S. J.; Yuk, T.; Kim, J.; Yoon, C. S.; Sun, Y. K. Variation of Electronic Conductivity within Secondary Particles Revealing a Capacity-Fading Mechanism of Layered Ni-Rich Cathode. *ACS Energy Letters* **2018**, 3 (12), 3002−3007.

(46) Tsai, P. C.; Wen, B.; Wolfman, M.; Choe, M. J.; Pan, M. S.; Su, L.; Thornton, K.; Cabana, J.; Chiang, Y. M. Single-Particle Measurements of Electrochemical Kinetics in NMC and NCA Cathodes for Li-Ion Batteries. *Energy Environ. Sci.* **2018**, 11 (4), 860−871.

(47) Woodford, W. H.; Carter, W. C.; Chiang, Y. M. Design Criteria for Electrochemical Shock Resistant Battery Electrodes. *Energy Environ. Sci.* **2012**, 5 (7), 8014−8024.

(48) Faenza, N. V.; Bruce, L.; Lebens-Higgins, Z. W.; Plitz, I.; Pereira, N.; Piper, L. F. J.; Amatucci, G. G. Growth of Ambient Induced Surface Impurity Species on Layered Positive Electrode Materials and Impact on Electrochemical Performance. *J. Electrochem. Soc.* **2017**, 164 (14), A3727−A3741.

(49) Liu, H.; Allan, P. K.; Borkiewicz, O. J.; Kurtz, C.; Grey, C. P.; Chapman, K. W.; Chupas, P. J. A Radially Accessible Tubular in Situ X-Ray Cell for Spatially Resolved Operando Scattering and Spectroscopic Studies of Electrochemical Energy Storage Devices. *J. Appl. Crystallogr.* **2016**, 49 (5), 1665−1673.

(50) Toby, B. H.; von Dreele, R. B. GSAS-II: The Genesis of a Modern Open-Source All Purpose Crystallography Software Package. *J. Appl. Crystallogr.* **2013**, 46, 544−549.